Energy & Environmental Science

ROYAL SOCIETY OF CHEMISTRY

PAPER

View Article Online
View Journal | View Issue

Cite this: *Energy Environ. Sci.*, 2022, **15**, 2557

A robust thermoelectric module based on MgAgSb/$Mg_3(Sb,Bi)_2$ with a conversion efficiency of 8.5% and a maximum cooling of 72 K†

Pingjun Ying,[a] Lennart Wilkens,[a] Heiko Reith,[a] Nicolas Perez Rodriguez,[a] Xiaochen Hong,[ab] Qiongqiong Lu,[a] Christian Hess,[ab] Kornelius Nielsch*[acd] and Ran He*[a]

The applications of thermoelectric (TE) technology around room temperature are monopolized by bismuth telluride (Bi_2Te_3). However, due to the toxicity and scarcity of tellurium (Te), it is vital to develop a next-generation technology to mitigate the potential bottleneck in raw material supply for a sustainable future. Hereby, we develop a Te-free n-type compound $Mg_3Sb_{0.6}Bi_{1.4}$ for near-room-temperature applications. A higher sintering temperature of up to 1073 K is found to be beneficial for reducing the electrical resistivity, but only if Mg is heavily overcompensated in the initial stoichiometry. The optimizations of processing and doping yield a high average zT of 1.1 in between 300 K and 573 K. Together with the p-type MgAgSb, we demonstrate module-level conversion efficiencies of 3% and 8.5% under temperature differences of 75 K and 260 K, respectively, and concomitantly a maximum cooling of 72 K when the module is used as a cooler. Besides, the module displays exceptional thermal robustness with a $<$ 10% loss of the output power after thermal cycling for $\sim$32 000 times between 323 K and 500 K. These proof-of-principle demonstrations will pave the way for robust, high-performance, and sustainable solid-state power generation and cooling to substitute highly scarce and toxic Bi_2Te_3.

Received 18th March 2022,
Accepted 26th April 2022

DOI: 10.1039/d2ee00883a

rsc.li/ees

Broader context

Thermoelectric (TE) technology – whereby heat is converted to electrical power and *vice versa* – holds great potential for cooling and power generation in many applications because its unique solid-state nature enables TE devices to be free from emissions and maintenance, thus providing extraordinary reliability. Realizing this potential requires developing modules that show high performance around room temperature (200 K to 600 K). Currently, almost all commercial modules are based on bismuth telluride (Bi_2Te_3) because of its unparalleled performance to date. However, Bi_2Te_3 cannot meet the rapidly increasing demand for TE technology, because tellurium (Te) is very scarce, with the Earth's crust having a concentration of $<$0.001 ppm. A sustainable solution that avoids the usage of the toxic and scarce element Te is currently missing for commercial TE modules, thus preventing the realization of the full potential of TE technology. This work tackles this challenge by generating a new paradigm for the realization of Te-free, sustainable, high-performance, and robust TE materials and modules using scalable processing approaches, thereby significantly advancing the sustainability of TE technology for both cooling and power generation applications.

1. Introduction

Despite the fact that the initial discovery was made as early as 1821, 201 year-old thermoelectric (TE) technology has experienced vigorous research and development activities in very recent decades, owing to the greatly increased demand for both sustainable energy sources and versatile cooling systems in our society. Utilizing the coupled transport of electrical current and heat flow in a solid-state, TE devices are noiseless, maintenance-free, and thus extremely reliable, as proven by the radioisotope thermoelectric generators (RTGs) that have powered space missions for decades. Therefore, TE technology promises solutions for both waste–heat recycling to electrical energy and spot cooling. Specifically, the application of TE technology around room temperature is of the highest interest. This is because: (1) for power generation, more than 60% of the energy generated by burning fossil fuels is dissipated as waste heat, of which more than half is low-grade heat with

[a] *Leibniz Institute for Solid State and Materials Research, 01069 Dresden, Germany. E-mail: k.nielsch@ifw-dresden.de, r.he@ifw-dresden.de*
[b] *School of Mathematics and Natural Sciences, University of Wuppertal, 42079, Wuppertal, Germany*
[c] *Institute of Materials Science, Technische Universität Dresden, 01062 Dresden, Germany*
[d] *Institute of Applied Physics, Technische Universität Dresden, 01062 Dresden, Germany*

† Electronic supplementary information (ESI) available. See DOI: https://doi.org/10.1039/d2ee00883a

temperatures <600 K;[1] (2) for cooling, the TE device outperforms the conventional vapor compression refrigerators in terms of cost and efficiency for small-scale (< 25 W) duties,[2] such as portable refrigerators, cooling laser diodes, high-performance electronics and radiation detectors, temperature control of car seats, *etc.*; (3) thermoelectric applications near room temperature constitute the largest and fastest growing sector of the future thermoelectric market including cooling for telecommunication, cryotherapy, and biomedicine, self-powered sensors for the nodes (quantity in trillions) of the internet-of-things (IoT), and waste heat recovery using low-grade heat.[3,4] Realizing these application potentials requires a TE technology that leads to high performance around room temperature, which further relies on the development of high-performance TE materials as well as adequately translating these materials into advanced modules and devices.

The performance of TE technology, either for cooling or power generation, is largely determined by the figure-of-merit (zT) of the materials, $zT = [(S^2/\rho)/(\kappa)]T$, where S, ρ, κ, and T are the Seebeck coefficient, electrical resistivity, thermal conductivity, and absolute temperature, respectively. The current state-of-the-art TE materials have shown average zT (zT_{ave}) values in the range of 0.8 to 1.2, which can be found in (1) Bi_2Te_3 around room temperature (200 K to 600 K); (2) skutterudites, Mg_2Si, and IV–VI compounds at intermediate temperatures (600 K to 800 K); (3) SiGe alloy and half-Heusler compounds at higher temperatures (800 K to 1200 K).[5] Many good TE materials, such as $FeSi_2$, SiGe, and half-Heusler compounds, have peak zT values of 0.6 to 1.5 between 900 K and 1200 K, but only 0.1 to 0.3 at room temperature.[6–9] Despite their exceptional robustness and applicability for industrial waste heat recovery, these materials are only suitable for heat sources with much higher temperatures, *e.g.* >700 K. The application of TE devices around room temperature is still dominated by Bi_2Te_3 for more than half a century. However, tellurium (Te) is an extremely scarce element with an abundance of less than 0.001 ppm (<0.0000001%) in the Earth's crust and an annual production of less than 500 metric tons globally.[10,11] This greatly challenges the near-future growth of the thermoelectric market, and it is imperative to develop TE modules that are free from the scarce and toxic elements while retaining a high performance at around room temperature.

In recent years, $Mg_3(Sb,Bi)_2$ intermetallic (so-called Zintl) compounds have attracted great attention because of their non-toxicity and elemental abundance. These compounds were studied as the p-type material for more than 10 years until Tamaki *et al.* in 2016 first reported the realization of the n-type material by adding excess Mg.[12] Subsequent investigations boomed, and a plethora of tailoring strategies have been proposed to advance their thermoelectric performances such as doping by various elements.[13] Besides, alloying Mg_3Bi_2 with Mg_3Sb_2 not only introduces point defects that can effectively scatter phonons but also modifies the band structure such as the bandgap and the energy positions of several pockets of the conduction band.[14] As a rule of thumb, a higher concentration of Bi shifts the peak zT towards a lower temperature, thus favoring applications at near room temperature. Particularly, one important strategy for improving the TE properties of $Mg_3(Sb,Bi)_2$ compounds is to reduce the grain-boundary scattering of electrons, which, in general, has been realized through (1) single crystal growth;[15] (2) post-annealing after sintering under a Mg-vapor atmosphere;[16] (3) introducing secondary phases (mostly elemental metals) to assist the grain growth.[17] These approaches successfully mitigated the grain boundary scattering of electrons to certain degrees, so the zT improved accordingly, especially at lower temperatures. However, the growth of single crystals and Mg-vapor annealing are usually time-consuming and can be complex, thus unsuitable for a scaled preparation of materials to facilitate their applications. Moreover, the inclusion of the secondary phase complicates microchemistry, and the mechanism of how these inclusions assist the grain growth remains unclear.

A much more straightforward and scalable strategy to increase the grain size is to apply a higher temperature during sintering, which has been reported to effectively enhance the charge carrier mobility and zT of $Mg_3(Sb,Bi)_2$ compounds. However, this approach has been dominantly applied to Sb-rich compounds, mostly $Mg_{3+\delta}Sb_{1.5}Bi_{0.5}$.[13,18] It remains less studied whether this approach is suitable for Bi-rich compounds. This is not a trivial question since the electrical properties of $Mg_{3.2}Bi_{1.5}Sb_{0.498}Te_{0.002}Cu_{0.01}$ were completely deteriorated by applying a sintering temperature of 1073 K, as reported by Liu *et al.*[19] However, 1073 K is usually a "safe" temperature for sintering Sb-rich compounds.[13,18,20] It is thus speculated that Bi-rich compounds are more prone to Mg evaporation upon heating, as can be rationalized by the fact that the melting point of Mg_3Bi_2 (~1094 K) is much lower than that of Mg_3Sb_2 (~1500 K), so the Mg atoms are more volatile in Bi-rich compounds than in Sb-rich ones. Therefore, it remains a great challenge to establish processing that can sinter Bi-rich $Mg_3(Sb,Bi)_2$ compounds at much higher temperatures while minimizing the Mg losses in the sintered body to enable an advanced TE performance.

Hereby, inspired by the work of Wood *et al.* where the applied Mg-vapor annealing could significantly improve the electrical transport,[16] and by the study of Imasato *et al.* where an n-to-p Seebeck transition was enabled by Mg-vapor annealing,[15] we propose to heavily compensate the Mg losses during sintering by adding 20% extra Mg in the initial stoichiometry, yielding a base compositional formula of $Mg_{3.6}Sb_{0.6}Bi_{1.4}$. This is different from many reports where the extra Mg did not exceed 10%. The high amount of extra Mg will compensate for its evaporation during sintering, which is similar to Mg-vapor annealing but realized in a single step. We found that this way, a higher sintering temperature of up to 1073 K successfully improves the electrical transport properties. Interestingly, we also found that such a high sintering temperature is unfavorable for a composition where the concentration of Mg is only 3.2 (*i.e.*, $Mg_{3.2}Sb_{0.6}Bi_{1.4}$), since the electrical performance degrades greatly. Using this synthesis approach, the TE properties are further optimized by changing the doping concentration. The peak zT values are enhanced to 0.74 at 300 K and

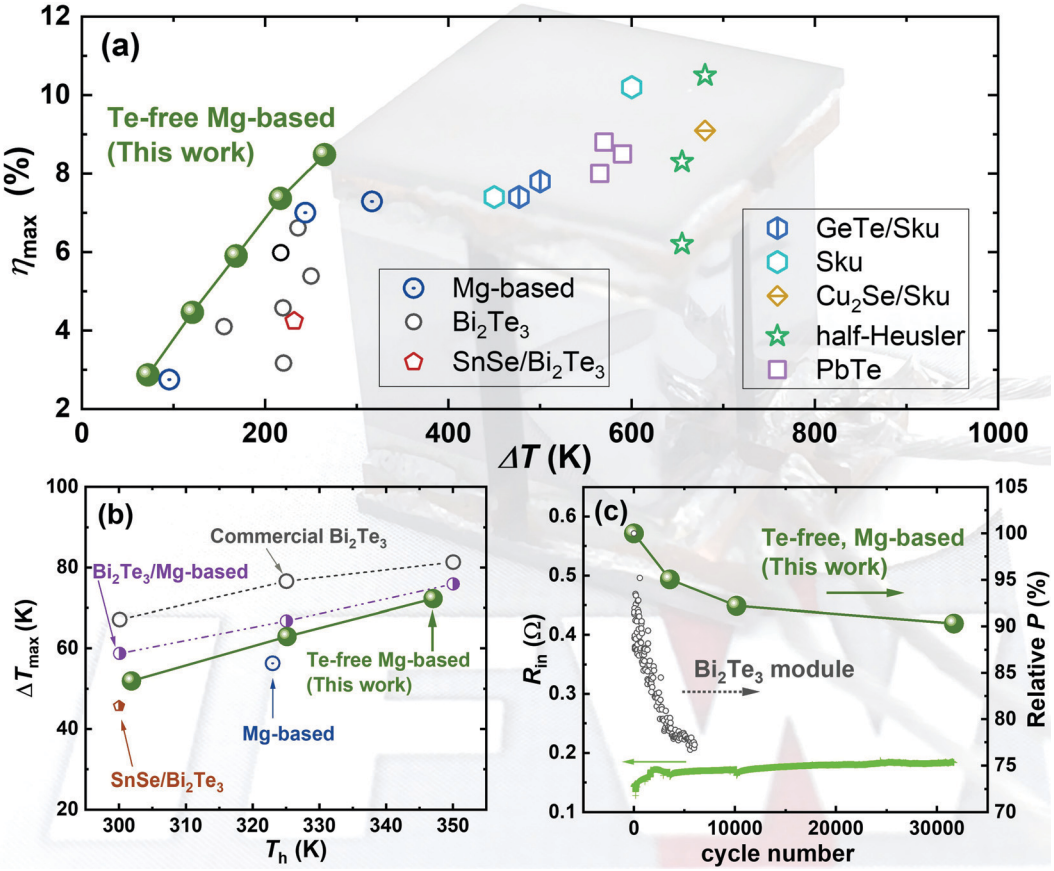

Fig. 1 Module performance for (a) power generation, (b) cooling, and (c) internal resistance (left) and the relative output power (right) upon thermal cycling based on Te-free compounds in this work including p-type $MgAg_{0.97}Sb_{0.99}$ and n-type $Mg_{3.6}Y_{0.003}Sb_{0.6}Bi_{1.4}$. The obtained maximum conversion efficiency (η_{max}), the cooling temperature (ΔT_{max}), and the relative output power are compared to other published results.[19,22–44] The abbreviation Sku represents skutterudite compounds. The cycling test of Bi_2Te_3 is based on a commercial Melcor HT9-3-25 module, where the cold side was fixed at 297 K and the hot side varied between 300 K and 473 K.[44]

1.24 at 453 K for $Mg_{3.6}Y_{0.003}Sb_{0.6}Bi_{1.4}$, resulting in a high average zT of 1.1 between 300 K and 573 K. The improved zT in this work is comparable or even exceeds the state-of-the-art n-type Bi_2Te_3 and other Bi-rich $Mg_3(Sb,Bi)_2$ compounds.[19,21,22] Subsequently, the optimized TE materials are translated into modules together with the p-type MgAgSb compound. The fabricated modules show excellent performances for both power generation and cooling. As shown in Fig. 1, for power generation, the conversion efficiencies reach 3% and 8.5% under temperature differences of 75 K and 260 K, respectively. For cooling, the maximum cooling ΔTs reach 52 K, 63 K, and 72 K with heat-rejection sides at 302 K, 325 K, and 347 K, respectively. These are comparable to or exceed the state-of-the-art modules.[19,22–43] Furthermore, we perform thermal cycling for a $Mg_3(Sb,Bi)_2$/MgAgSb module by exposing the hot side between 323 K and 500 K continuously while maintaining the cold side at 288 K. We found that the loss in the relative output power is less than 10% after ~32 000 times cycling (~5000 hours equivalence). The cycling performance outperforms the Bi_2Te_3-based module[44] and unveils the great thermal robustness of our module. Our realizations are the first demonstration of an exceptionally robust thermoelectric module that is completely free from toxic and scarce elements for both high-performance power generation and cooling. The Mg-based technology thus promises the great potential to break the room-temperature monopoly of Bi_2Te_3 that has lasted for more than half a century.

2. Results and discussion

2.1 The TE properties of heavily overcompensated $Mg_{3.6}Y_{0.003}Sb_{0.6}Bi_{1.4}$

The details of material synthesis, thermoelectric property measurements, sample characterization, module fabrication, and the measurement of efficiency and cooling are given in the ESI† (Section A). In this work, yttrium (Y) is selected as the dopant to completely eliminate Te. Besides, doping by Y is more suitable for application than that by Te since the former enables a much better thermal stability upon aging, which might be understood by the higher melting point and lower vapor pressure of Y than those of Te.[45] To study the effect of the sintering temperature, we selected a composition $Mg_{3.6}Y_{0.003}Sb_{0.6}Bi_{1.4}$ and sintered it at 973 K, 1023 K, and 1073 K, respectively. Their thermoelectric

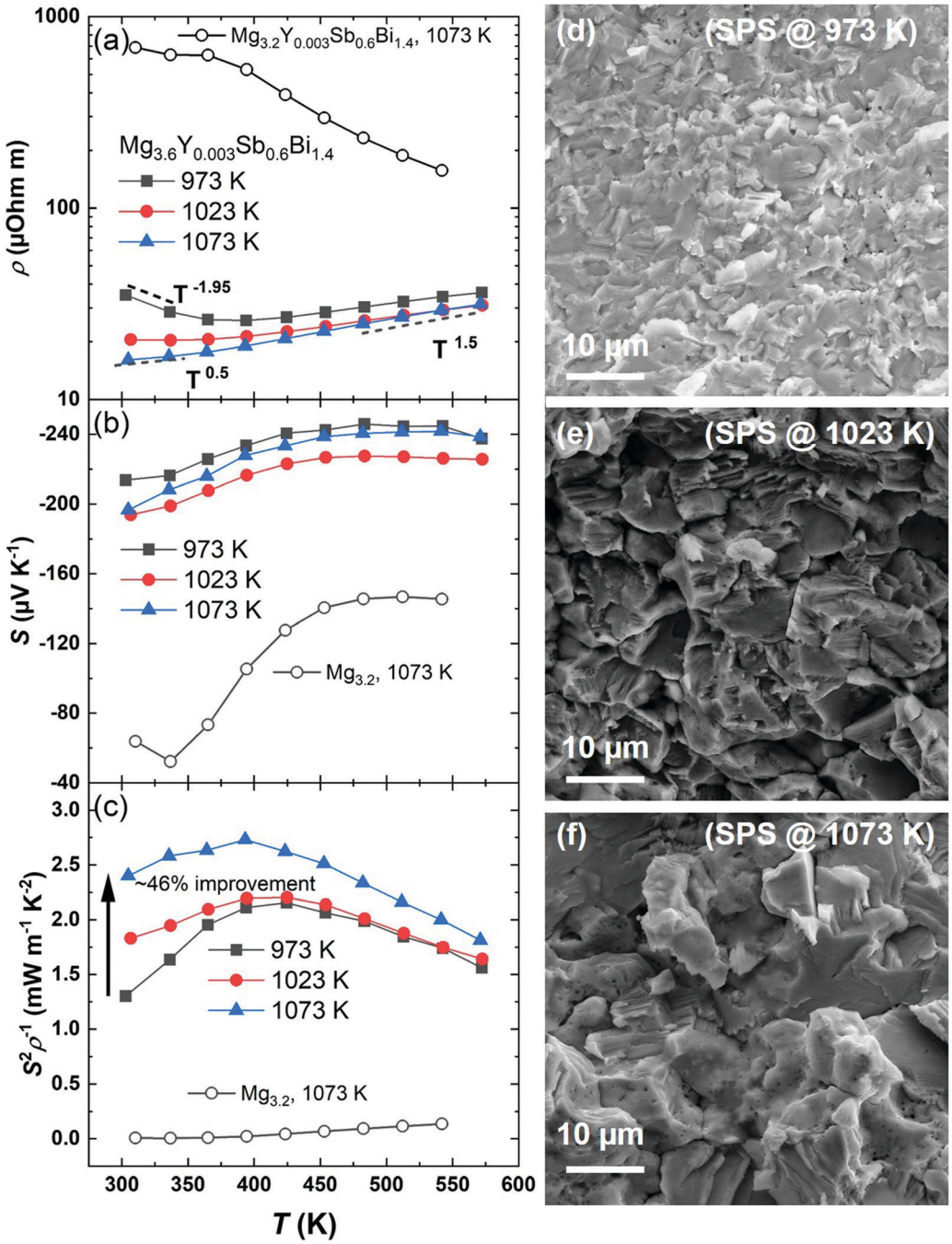

Fig. 2 Temperature-dependent (a) electrical resistivity, (b) Seebeck coefficient, (c) power factor, and (d–f) the SEM images of $Mg_{3.6}Y_{0.003}Sb_{0.6}Bi_{1.4}$ that are sintered at 973 K, 1023 K, and 1073 K. The electronic transport data of $Mg_{3.2}Y_{0.003}Sb_{0.6}Bi_{1.4}$ are plotted for comparison.

performances are shown in Fig. 2. We found that the sintering temperature has a significant effect on reducing the electrical resistivity, especially at lower temperatures, as shown in Fig. 2a. For example, the resistivity shows a ~54% reduction from ~35 μOhm m to ~16 μOhm m by increasing the sintering temperature from 973 K to 1073 K. The sintering temperature also modifies the scattering mechanism. At higher temperatures, all samples roughly follow a $\rho \sim T^{1.5}$ relationship, indicating that the charge carriers are scattered by acoustic phonons. Meanwhile, at lower temperatures, the sample sintered at 973 K shows a negative trend, *i.e.*, $\rho \sim T^{-1.95}$, whereas the sample sintered at 1023 K and 1073 K displays the relationships of $\rho \sim T^{-0.1}$ and $\rho \sim T^{0.5}$, respectively, suggesting the concerting of the grain boundaries with acoustic phonons for scattering charge carriers.[46,47]

Fig. 2b shows that the Seebeck coefficient changes slightly with respect to the sintering temperature. The use of a higher sintering temperature, to 1073 K, is thus demonstrated to be

effective for improving the power factor ($S^2\rho^{-1}$) by ~46% at room temperature when compared to the one sintered at 973 K, as shown in Fig. 2c. Notably, such a high sintering temperature is applicable only if Mg is heavily compensated in the initial composition ($Mg_{3.6}Y_{0.003}Sb_{0.6}Bi_{1.4}$). This is clarified by sintering another compound at 1073 K with less excess Mg, *i.e.*, $Mg_{3.2}Y_{0.003}Sb_{0.6}Bi_{1.4}$. We found a drastically higher resistivity together with a greatly reduced Seebeck coefficient if the amount of Mg is only 3.2, as shown in Fig. 2. These results manifest the Mg-poor conditions – a known performance killer for the n-type $Mg_3(Sb,Bi)_2$. The beneficial effects of the heavily compensated Mg are thus confirmed in maintaining Mg-rich conditions and in improving the electronic conductivity. The improving mechanism in our work is similar to that of Wood *et al.*, where a higher conductivity was realized through post-annealing in Mg vapor for 65 hours.[16] Despite the interesting findings, post-annealing not only adds an extra step to complicate and prolong the processing, but may also have insignificant effects if the sintered wafers are thick or if they are sandwiched between contact layers. In this work, we realize a similarly improved conductivity in just one step that will not encounter the thickness or contact issues. This aspect is important for the development of high-performance n-type Bi-rich $Mg_3(Sb,Bi)_2$ compounds on a larger scale with higher reproducibility to facilitate their applications.

The variations in the electronic transport properties are correlated with the microstructures. The X-ray diffraction patterns of the as-prepared specimens in this work are shown in the ESI† (Fig. S1). It is surprising to see that the addition of such a high amount of excessive Mg (~20%) does not introduce impurity peaks. In fact, the peaks of a commonly observed impurity phase, Bi, do not appear in the XRD patterns in this work. This can be explained by the employed higher sintering temperatures that promote the reaction among the constituent elements, and the excessively added Mg guarantees the elemental supply despite its evaporation. In addition, Fig. 2d, e, and f show the scanning electron microscopy (SEM) images of the freshly broken surfaces of the $Mg_{3.6}Y_{0.003}Sb_{0.6}Bi_{1.4}$ samples sintered at 973 K, 1023 K, and 1073 K, respectively. The enlargement of the grains is found, which is responsible for the reduced electrical resistivity, especially at near room temperature. The observed grain growth stems from an increased atomic diffusion due to the higher sintering temperature. Despite the grain enlargement, the sample with the largest grains in this work still displays a $\rho \sim T^{0.5}$ relationship at near room temperature, which indicate the possibility of a subsequently improving the electrical transport upon further grain growth by, for example, adding more Mg in the initial composition and applying a higher sintering temperature. Indeed, a $\rho \sim T^{1.5}$ relationship has been found even at room temperature in a grain-boundary-free sample, *i.e.*, a single crystal.[14]

2.2 Thermoelectric performance of $Mg_{3.6}Y_xSb_{0.6}Bi_{1.4}$

Based on the optimized processing conditions, we further modify the amount of Y, a trivalent dopant, to change the carrier concentration. The full-set thermoelectric transport properties of compositions $Mg_{3.6}Y_xSb_{0.6}Bi_{1.4}$ with x = 0.001, 0.002, 0.003, 0.004, and 0.005 are characterized and shown in Fig. 3. The electrical resistivity is found to decrease by increasing the concentration of Y. Besides, the increased power law of $\rho \sim T^{1.88}$ is found for the compounds with the highest usage of Y (x = 0.005) at elevated temperatures. The exponent is larger than 1.5, suggesting that the electrical resistivity is influenced not only by acoustic phonon scattering. As will be shown later, the larger-than-1.5 exponent originates from an anomalously decreased Hall carrier concentration (n_H) upon heating, whereas the Hall mobility (μ_H) still follows a $\mu_H \sim T^{-1.5}$ relationship at higher temperatures. Furthermore, the exponent is found to decrease by either reducing the temperature or reducing the concentration of Y, which manifests the impacts of grain boundary scattering. Note that, for the compound with x = 0.001, the observed negative dependence of $\rho \sim T^{-0.1}$ at ~550 K originates from the bipolar excitation.

The decrease in the resistivity is accompanied by the decrease in the Seebeck coefficient, as shown in the right axis in Fig. 3a. Besides, the temperature where the Seebeck coefficient peak appears displays a decreasing trend with a lower content of Y. This indicates an earlier onset of bipolar excitation with the decreased doping level. To understand the variations in both the resistivity and the Seebeck coefficient, we performed the Hall measurement for the Y-doped compounds from room temperature up to 468 K. The temperature-dependent Hall carrier concentration (n_H) is found in Fig. 3b. The enhanced Y concentration yields an increase in n_H. Furthermore, as is more clearly shown in the ESI† (Fig. S2), the n_H curves display an increasing trend for x = 0.001 and x = 0.002 that is correlated with bipolar excitation. Interestingly, while n_H is nearly constant for x = 0.003 and x = 0.004, it displays an anomalous decreasing trend for x = 0.005 upon heating. We note that a similar decrease in n_H was also reported for the Sb-rich compound, $Mg_{3.2}Sb_{1.5}Bi_{0.49}Te_{0.01}$.[48] The decreased n_H with a higher temperature is not very well understood but might be related to the thermodynamic equilibrium concentration of Mg vacancies that depends on the temperature.[48] This also agrees with the prerequisite of Mg-rich growth conditions to enable a higher doping efficiency for n-type $Mg_3(Sb,Bi)_2$. Furthermore, based on the measured n_H and electrical resistivity (ρ), the temperature-dependent Hall mobility (μ_H) is evaluated using $\mu_H = 1/\rho n_H e$ (e is the positive value of the electron charge). The μ_H shows a weak dependence on the dopant concentration, as shown in Fig. 3b. Besides, μ_H decreases with a temperature from ~180 $cm^2\ V^{-1}\ s^{-2}$ at 300 K to ~120 $cm^2\ V^{-1}\ s^{-2}$ at 450 K due to the acoustic phonon scattering that intensifies upon heating.

To further understand the electronic transport properties, we evaluate the density-of-state effective masses (m_{DOS}) of the charge carriers by plotting the Seebeck coefficient *vs.* n_H, *i.e.*, through the Pisarenko relationship, $|S| = \frac{8\pi^2 k_B^2 T}{3eh^2}\left(\frac{\pi}{3n_H}\right)^{2/3} m_{DOS}$, where k_B is the Boltzmann constant and h is the Planck constant. Note that although this expression is assumed for carriers under the acoustic phonon

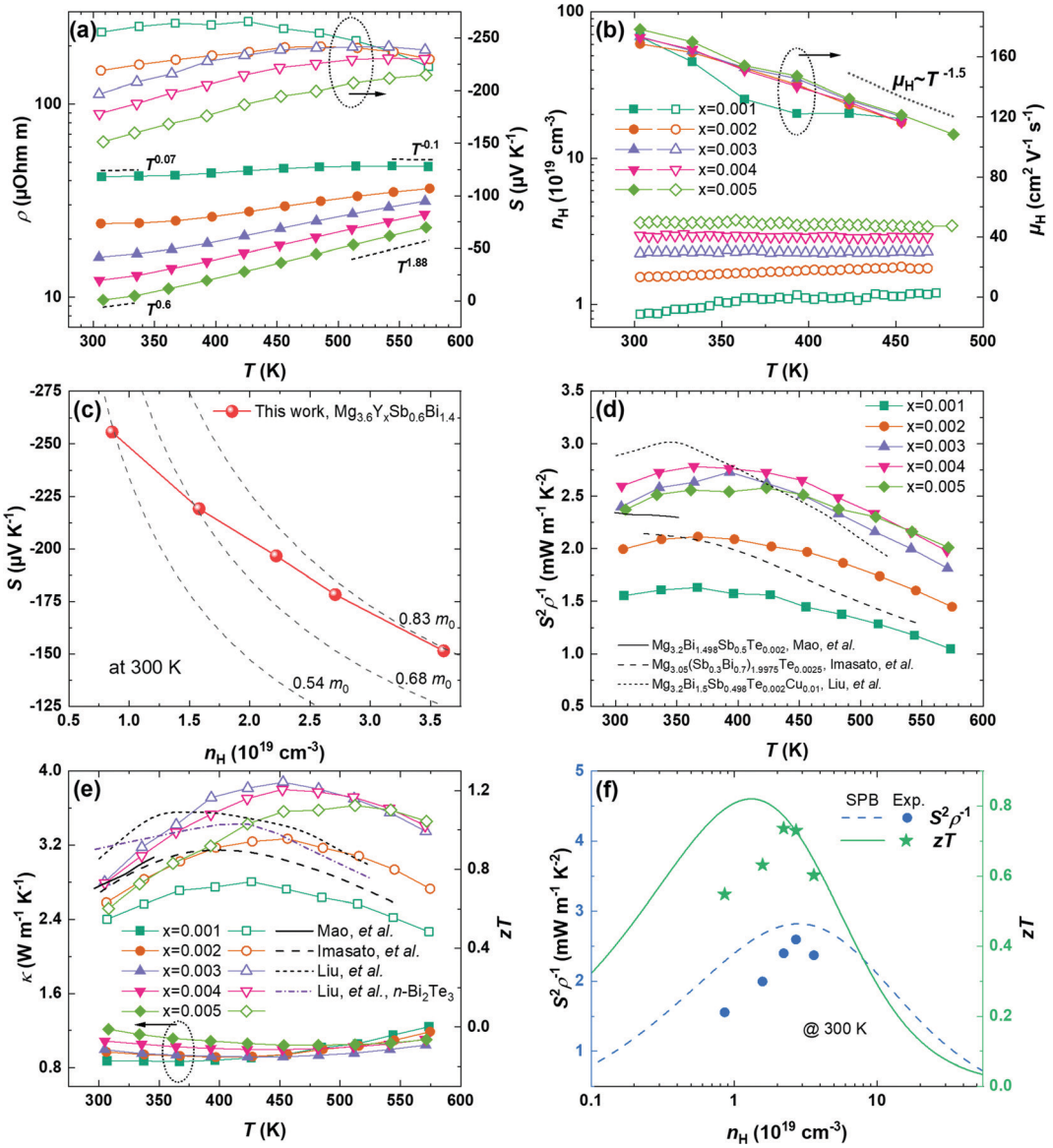

Fig. 3 Thermoelectric transport properties of $Mg_{3.6}Y_xSb_{0.6}Bi_{1.4}$ with x = 0.001, 0.002, 0.003, 0.004, and 0.005. (a) Temperature-dependent (left) electrical resistivity and (right) Seebeck coefficient. (b) Temperature-dependent (left) carrier concentration and (right) mobility. (c) Pisarenko relationship (*i.e.*, Seebeck coefficient *vs.* the carrier concentration) at 300 K. (d) Temperature-dependent power factor. (e) Temperature-dependent (left) thermal conductivity and (right) zT. (f) Analysis of the (left) power factor and (right) zT at 300 K using the single parabolic band (SPB) model. The power factor and zT are compared to literature studies.[19,21,22]

scattering, it also applies in the presence of grain boundary scattering since both the Seebeck coefficient and the carrier concentration have weak dependences on the grain sizes, at least for the specimens where the grains are not extremely refined. The insensitivity of the carrier concentration and the Seebeck coefficient to the grain boundary scattering was reported for various thermoelectric materials such as $Mg_{3.2}Sb_{1.5}Bi_{0.5}$ and half-Heusler NbFeSb.[13,49] A gradual increase in m_{DOS} from ~0.54 m_0 to ~0.83 m_0 is found by increasing x from 0.001 to 0.005, as shown in Fig. 3c. Note that $m_{DOS} = m_b (N_V)^{2/3}$, where m_b is the band effective mass and N_V is the number of valley degeneracy in the conduction band. Since the mobility shows an insignificant variation with the doping level (except for x = 0.001 at higher temperatures where the single-band assumption is less valid), m_b experiences minor change and can be reasonably assumed as the constant. Then, the increased m_{DOS} can be solely ascribed to an enhanced N_V by a factor of ~2, as shown in the ESI† (Fig. S3), indicating a gradual involvement of higher-energy pockets for electron transport when the Fermi level is moved deeper inside the conduction band. This is consistent with the calculation of Imasato *et al.* where the conduction band of $Mg_3(Sb,Bi)_2$ possesses a multi-valley nature, and the differences in the band-edge energies of these pockets are reduced by mixing Bi and Sb.[14]

Using the electrical resistivity and the Seebeck coefficient, the temperature-dependent power factors (PF, $S^2\rho^{-1}$) of $Mg_{3.6}Y_xSb_{0.6}Bi_{1.4}$ are evaluated and shown in Fig. 3d. An improvement in the PF is realized by optimizing the doping

level. For example, the PF is $\sim$1.6 mW m^{-1} K^{-2} with x = 0.001 at room temperature; it increases to 2.6 mW m^{-1} K^{-2} for x = 0.004, and further reaches a peak value of $\sim$2.8 mW m^{-1} K^{-2} at 363 K. We also plot the PF from other reports among the Bi-rich n-type $Mg_3(Sb,Bi)_2$ compounds that are more suitable for applications at near room temperature. In general, the PF realized in this work is better than others except for the recent work of Liu *et al.* where a slightly higher PF at lower temperatures was achieved.[19] This is ascribed to the addition of Cu that effectively assisted the grain growth during sintering, which should also be complementary to the heavy-compensation strategy in this work and will be studied in the future. On the other hand, the achieved PF in this work is higher than that of Liu *et al.* at above 393 K, so the average PF is similar. In addition, Fig. 3e shows that the thermal conductivity displays an increasing trend by increasing the concentration of Y, which originates from the electronic thermal conductivity due to the reduced electrical resistivity.

The thermal conductivity values of the materials prepared in this work are small, with the lowest value reaching $\sim$0.8 W m^{-1} K^{-2} for $Mg_{3.6}Y_{0.001}Sb_{0.6}Bi_{1.4}$. Ultimately, the zT value in this work has been improved with the highest values reaching 0.74 at 300 K and 1.24 at 453 K for $Mg_{3.6}Y_{0.003}Sb_{0.6}Bi_{1.4}$, yielding a high average zT of 1.1 in between 300 K and 573 K. Fig. 3f shows the n_H-dependent PF and zT at 300 K using a single parabolic band (SPB) model.[50] Note that the modeling assumes a constant effective mass of 0.7 m_0 that is averaged among these compounds, and that the charge carriers are scattered by the acoustic phonons only. We found that the experimental zT value agrees well with the SPB model if the carrier concentration is sufficiently high ($n_H > 2 \times 10^{19}$ cm^{-2}). For the less doped compounds, the experimental zT value is slightly lower than the SPB-model predictions. These results manifest the impacts of the grain boundary scattering and suggest that further zT improvement is feasible by eliminating the grain boundary scattering in a compound with a slightly lower carrier concentration. In comparison to the n-type Bi_2Te_3 and Bi-rich n-type $Mg_3(Sb,Bi)_2$, our work achieves a comparable zT at room temperature,[19,21,22,51] showing its great potential for cooling applications. Besides, at temperatures higher than 393 K, our material displays a better zT than many other reports, suggesting its potential to enable a higher conversion efficiency when integrating the as-prepared materials into power-generation and cooling modules.

2.3 Te-free TE module for both power generation and cooling

Using the thermoelectric material with the optimized zT, *i.e.*, $Mg_{3.6}Y_{0.003}Sb_{0.6}Bi_{1.4}$, we further fabricate modules with $MgAg_{0.97}Sb_{0.99}$ as the p-type leg. The thermoelectric performance of the p-type is shown in the ESI† (Fig. S4). The materials employed in this work rival the best-performing state-of-the-art Bi_2Te_3 materials, but without using any elements that are scarce and toxic. Besides, as shown in Fig. 1, the Mg-based modules display a <10% reduction in the relative output power after thermal cycling the hot side between 323 K and 500 K for $\sim$ 32 000 times while maintaining the cold side at 288 K. In comparison, the Bi_2Te_3 modules display faster degradation by $\sim$25% after 6000 cycles, under less-severe cycling conditions with a varying hot side between 297 K and 473 K, as shown in Fig. 1c. These results suggest the great robustness of the Mg-based compounds and modules. The degradation of the output power can be understood by the mismatched coefficient of thermal expansion (CTE). In this work, we use silver (Ag) and iron (Fe) as the contact materials for p- and n-type legs, respectively, and prepare the contact bonding using one-step sintering. More details on contact-making and the elemental mapping can be found in the ESI† (Fig. S5 and S6). Although the CTE difference between the p-type MgAgSb ($\sim 19 \times 10^{-6}$ K^{-1}) and Ag ($\sim 20 \times 10^{-6}$ K^{-1}) is small, it is much larger between the n-type $Mg_3(Sb,Bi)_2$ (22×10^{-6} K^{-1}) and Fe ($\sim 12 \times 10^{-6}$ K^{-1}). The long-term heating/cooling cycling will thus create residual stress and the pile-up of dislocations due to the hysteresis of tensile/compressive stresses. This will increase the interfacial resistance and decrease the output power. Furthermore, the lower contact resistance is extremely important to reduce the electrical energy losses to enable a higher conversion efficiency (η) and an output power (P). The contact resistivities can be reasonably assumed to be identical to our previous work,[23] where the respective values are $\sim$6 μOhm cm^2 for Ag/$MgAg_{0.97}Sb_{0.99}$ and $\sim$26.6 μOhm cm^2 for Fe/$Mg_{3.6}Y_{0.003}Sb_{0.6}Bi_{1.4}$. A cross-sectional area of 4 × 4 mm^2 for both legs is also applied to the module herein.

Fig. 4a shows the measured current–voltage (I–V) curves for the power generation modules under various temperature differences (ΔT). A good linearity is obtained and based on which the module's internal resistance and the open-circuit voltage are evaluated using the slope and intercept, and the results are given in the ESI† (Fig. S7). P is plotted in the right axis of Fig. 4a, where the peak corresponds to the matched impedance condition where the internal resistance and the load resistance are equal. Moreover, the measured current-dependent heat flow ($Q_{meas.}$) at a series of ΔT, as well as the simulated temperature distribution, is plotted in the ESI† (Fig. S8 and S9, respectively). The $Q_{meas.}$ values are only slightly higher ($\sim$5%) than the simulated heat flow ($Q_{sim.}$), indicating that our module design successfully minimized the thermal radiation energy losses. Subsequently, the current-dependent heat-to-power conversion efficiency (η) is evaluated under a series of ΔT, as shown in Fig. 4b. The η_{max} value increases with the ΔT, and a peak η_{max} of 8.5% is achieved under a ΔT of 260 K, as shown in Fig. 1a. The obtained efficiency exceeds all the Bi_2Te_3-based modules that are openly published to the authors' knowledge. More interestingly, due to the improved zT at near room temperature, we achieved a high efficiency of 3% at a mild ΔT of 75 K. Hence, our obtained module is ideal for application using low-grade heat sources where the heat flow is small.

Because of the module's excellent thermoelectric performance at near room temperature, we further investigate its cooling performance. The theoretical maximum cooling performance is evaluated based on the finite-element simulation (FEM) using COMSOL. The temperature distribution of the

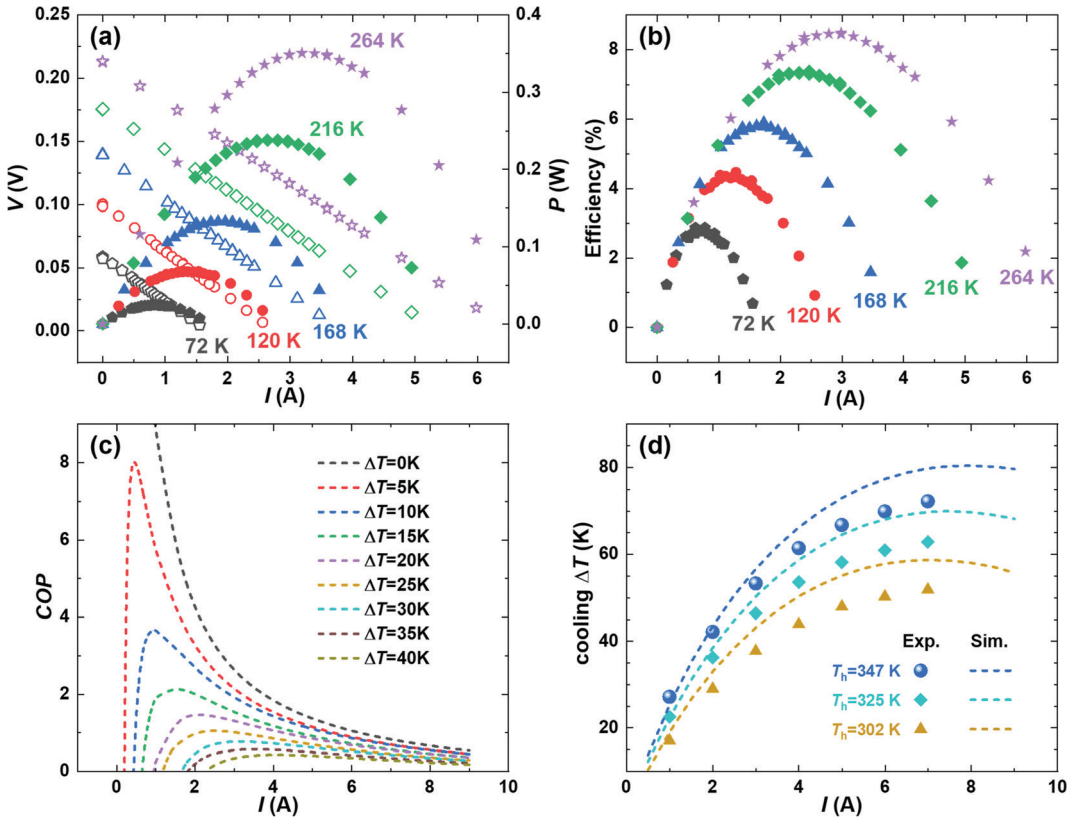

Fig. 4 Current (*I*)-dependent (a) output voltage (left, *V*), power (right, *P*), and (b) efficiency (η) under a variety of applied temperature differences for the power-generation module. The current (*I*)-dependent (c) COP with a hot-side temperature of 325 K and (d) cooling ΔT for the cooling module.

modules under the cooling mode is shown in the ESI† (Fig. S9). In the future, we will use FEM to further optimize the geometrical configurations to advance the module-level performance, as has been similarly realized in designing power-generation modules.[52] In addition, Fig. 4c gives the simulated coefficient of performance (COP) with a hot-side temperature of 325 K. The COP represents the amount of heat pumped divided by the amount of the supplied electrical power. Unfortunately, the experimental COP cannot be evaluated in this work due to the lack of heat-flow-measurement capability in our measurement setup. The measurement setup will be upgraded in the future with the installation of heaters and heat-flux sensors. Nevertheless, the cooling ΔT can be simulated and measured, and compared, as shown in Fig. 4d. With the increasing current, the cooling ΔT increases until it reaches a maximum and then decreases again. Such a current-dependent ΔT curve stems from the interplay among several effects including heat conduction, the Peltier cooling, the Joule heating, and the Thomson effect. The theoretical maximum cooling ΔT reaches 58 K, 70 K, and 80 K with heat-rejection sides at 302 K, 325 K, and 347 K, respectively, which are slightly higher than the experimental numbers that are 52 K, 63 K, and 72 K, respectively. Considering the high vacuum ($\sim 10^{-7}$ mbar) and the relatively low temperature, heat losses from radiation or convection should be negligible. Therefore, we speculate the experimentally reduced cooling ΔT has two possible origins: (1) electrical losses between the contact/thermoelectric materials and the brazing points for wiring. (2) The inaccurate simulation since the low-temperature transport properties are not directly measured, instead they are extrapolated using the data from room temperature and above. In the future, we will address these issues to further understand and boost the cooling performance by, *e.g.*, measuring and improving the low-temperature properties of materials. Nevertheless, the realized cooling is comparable to commercial Bi_2Te_3-based modules,[22] thus showing great promise in developing the Te-free thermoelectric technology for near-room-temperature cooling applications.

3. Summary

In summary, the thermoelectric performance of Bi-rich n-type $Mg_{3.6}Y_xSb_{0.6}Bi_{1.4}$ compounds is improved by using a higher sintering temperature of 1073 K to effectively mitigate the grain-boundary scattering of charge carriers. The importance of a heavily compensated Mg content in the starting composition for the high-temperature sintering strategy is revealed, as otherwise the electrical properties will degrade significantly due to the evaporation of Mg. By further modifying the dopant concentration, the *zT* is enhanced to 0.74 at 300 K and 1.24 at 453 K for $Mg_{3.6}Y_{0.003}Sb_{0.6}Bi_{1.4}$, yielding a high average *zT* of

1.1 between 300 K and 573 K. The improved materials are further translated into modules together with the p-type $MgAg_{0.97}Sb_{0.99}$. For the power generation module, high heat-to-power conversion efficiencies of 3% and 8.5% are achieved under ΔTs of 75 K and 260 K, respectively. For the cooling module, maximum cooling ΔTs of 52 K, 63 K, and 72 K are achieved with hot sides fixed at 302 K, 325 K, and 347 K, respectively. Furthermore, the module displays excellent thermal cycling stability with a reduction in the relative output power of less than 10% after ~32 000 cycles between 323 K and 500 K. This work successfully illustrates, for the first time, the module-level performances using TE materials that are based on sustainable and environmentally benign elements for both power generation and cooling around room temperature, while retaining exceptional robustness to thermal cycling. This work shows the great potential of developing a new thermoelectric paradigm, using materials that are completely free from elements that are toxic and scarce to meet the rapidly increasing demand for thermoelectric technology not only in niche applications but also in the consumer market in the near future.

Author contributions

K. N. and R. H. designed the research; P. Y. and R. H. synthesized the materials; P. Y. fabricated the devices and measured the conversion efficiency; P. Y. formed the FEM simulation; L. W. and H. R. assembled the instrument for cooling measurements; P. Y. and L. W. measured the cooling performance; N. P. conducted the Hall measurement; X. H. and C. H. contributed analytical tools; Q. L. conducted the SEM characterization; P. Y., R. H. and K. N. prepared the manuscript; and all the authors commented on the manuscript.

Conflicts of interest

The authors declare no conflicts of interest.

Acknowledgements

We greatly acknowledge financial support by the strategic project at IFW Dresden on ''Wireless sensor devices for high temperature applications''. RH acknowledges financial support from the Deutsche Forschungsgemeinschaft (DFG), Project Number 453261231. Thanks to Ms Juliane Scheiter for her support on the Hall measurement.

References

1 G. Schierning, *Nat. Energy*, 2018, **3**, 92–93.
2 J. Mao, G. Chen and Z. Ren, *Nat. Mater.*, 2020, **20**, 454–461.
3 D. Champier, *Energy Convers. Manage.*, 2017, **140**, 167–181.
4 *Thermoelectric Coolers Market by Model, Design, and End-User Industry: Global Opportunity Analysis and Industry Forecast, 2021-2030*, 2021.
5 R. He, W. Heyn, F. Thiel, N. Pérez, C. Damm, D. Pohl, B. Rellinghaus, C. Reimann, M. Beier, J. Friedrich, H. Zhu, Z. Ren, K. Nielsch and G. Schierning, *J. Materiomics*, 2019, **5**, 15–33.
6 H. Zhu, R. He, J. Mao, Q. Zhu, C. Li, J. Sun, W. Ren, Y. Wang, Z. Liu, Z. Tang, A. Sotnikov, Z. Wang, D. Broido, D. J. Singh, G. Chen, K. Nielsch and Z. Ren, *Nat. Commun.*, 2018, **9**, 2497.
7 J. Yu, C. Fu, Y. Liu, K. Xia, U. Aydemir, T. C. Chasapis, G. J. Snyder, X. Zhao and T. Zhu, *Adv. Energy Mater.*, 2017, **8**, 1701313.
8 G. Joshi, H. Lee, Y. Lan, X. Wang, G. Zhu, D. Wang, R. W. Gould, D. C. Cuff, M. Y. Tang, M. S. Dresselhaus, G. Chen and Z. Ren, *Nano Lett.*, 2008, **8**, 4670–4674.
9 P. Qiu, J. Cheng, J. Chai, X. Du, X. Xia, C. Ming, C. Zhu, J. Yang, Y. Y. Sun, F. Xu, X. Shi and L. Chen, *Adv. Energy Mater.*, 2022, **12**, 2200247.
10 S. R. Taylor, *Geochim. Cosmochim. Acta*, 1964, **28**, 1273–1285.
11 R. J. Goldfarb, 2015, DOI: **10.3133/fs20143077**.
12 H. Tamaki, H. K. Sato and T. Kanno, *Adv. Mater.*, 2016, **28**, 10182–10187.
13 K. Liu, C. Chen, X. Li, J. Jia, C. Xia, J. Mao, Q. Huang, J. Sui, F. Cao, X. Liu, Y. Chen and Q. Zhang, *ACS Appl. Mater. Interfaces*, 2022, **14**, 7022–7029.
14 K. Imasato, S. D. Kang, S. Ohno and G. J. Snyder, *Mater. Horiz.*, 2018, **5**, 59–64.
15 K. Imasato, C. Fu, Y. Pan, M. Wood, J. J. Kuo, C. Felser and G. J. Snyder, *Adv. Mater.*, 2020, **32**, 1908218.
16 M. Wood, J. J. Kuo, K. Imasato and G. J. Snyder, *Adv. Mater.*, 2019, **31**, 1902337.
17 T. Luo, J. J. Kuo, K. J. Griffith, K. Imasato, O. Cojocaru-Mirédin, M. Wuttig, B. Gault, Y. Yu and G. J. Snyder, *Adv. Funct. Mater.*, 2021, **31**, 2100258.
18 X. Chen, J. Zhu, D. Qin, N. Qu, W. Xue, Y. Wang, Q. Zhang, W. Cai, F. Guo and J. Sui, *Sci. China Mater.*, 2021, **64**, 1761–1769.
19 Z. Liu, W. Gao, H. Oshima, K. Nagase, C.-H. Lee and T. Mori, *Nat. Commun.*, 2022, **13**, 1120.
20 J. Zhang, L. Song, K. A. Borup, M. R.-V. Jørgensen and B. B. Iversen, *Adv. Energy Mater.*, 2018, **8**, 1702776.
21 K. Imasato, S. D. Kang and G. J. Snyder, *Energy Environ. Sci.*, 2019, **12**, 965–971.
22 J. Mao, H. Zhu, Z. Ding, Z. Liu, G. A. Gamage, G. Chen and Z. Ren, *Science*, 2019, **365**, 495–498.
23 P. Ying, R. He, J. Mao, Q. Zhang, H. Reith, J. Sui, Z. Ren, K. Nielsch and G. Schierning, *Nat. Commun.*, 2021, **12**, 1121.
24 R. Deng, X. Su, S. Hao, Z. Zheng, M. Zhang, H. Xie, W. Liu, Y. Yan, C. Wolverton, C. Uher, M. G. Kanatzidis and X. Tang, *Energy Environ. Sci.*, 2018, **11**, 1520–1535.
25 F. Hao, P. Qiu, Y. Tang, S. Bai, T. Xing, H.-S. Chu, Q. Zhang, P. Lu, T. Zhang, D. Ren, J. Chen, X. Shi and L. Chen, *Energy Environ. Sci.*, 2016, **9**, 3120–3127.
26 X. Hu, K. Nagase, P. Jood, M. Ohta and A. Yamamoto, *J. Electron. Mater.*, 2015, **44**, 1785–1790.
27 T. Kuroki, K. Kabeya, K. Makino, T. Kajihara, H. Kaibe, H. Hachiuma, H. Matsuno and A. Fujibayashi, *J. Electron. Mater.*, 2014, **43**, 2405–2410.

28 S. Wang, W. Xie, H. Li and X. Tang, *Intermetallics*, 2011, **19**, 1024–1031.
29 Z. Liu, N. Sato, W. Gao, K. Yubuta, N. Kawamoto, M. Mitome, K. Kurashima, Y. Owada, K. Nagase, C.-H. Lee, J. Yi, K. Tsuchiya and T. Mori, *Joule*, 2021, **5**, 1196–1208.
30 J. Yang, G. Li, H. Zhu, N. Chen, T. Lu, J. Gao, L. Guo, J. Xiang, P. Sun, Y. Yao, R. Yang and H. Zhao, *Joule*, 2022, **6**, 193–204.
31 B. Qin, D. Wang, X. Liu, Y. Qin, J.-F. Dong, J. Luo, J.-W. Li, W. Liu, G. Tan, X. Tang, J.-F. Li, J. He and L.-D. Zhao, *Science*, 2021, **373**, 556–561.
32 **https://hi-z.com/**, (accessed 17.03, 2022).
33 G. Bai, Y. Yu, X. Wu, J. Li, Y. Xie, L. Hu, F. Liu, M. Wuttig, O. Cojocaru-Mirédin and C. Zhang, *Adv. Energy Mater.*, 2021, **11**, 2102012.
34 J. Chu, J. Huang, R. Liu, J. Liao, X. Xia, Q. Zhang, C. Wang, M. Gu, S. Bai, X. Shi and L. Chen, *Nat. Commun.*, 2020, **11**, 2723.
35 S. El Oualid, I. Kogut, M. Benyahia, E. Geczi, U. Kruck, F. Kosior, P. Masschelein, C. Candolfi, A. Dauscher, J. D. Koenig, A. Jacquot, T. Caillat, E. Alleno and B. Lenoir, *Adv. Energy Mater.*, 2021, **11**, 2100580.
36 C. Fu, S. Bai, Y. Liu, Y. Tang, L. Chen, X. Zhao and T. Zhu, *Nat. Commun.*, 2015, **6**, 8144.
37 X. Hu, P. Jood, M. Ohta, M. Kunii, K. Nagase, H. Nishiate, M. G. Kanatzidis and A. Yamamoto, *Energy Environ. Sci.*, 2016, **9**, 517–529.
38 B. Jiang, X. Liu, Q. Wang, J. Cui, B. Jia, Y. Zhu, J. Feng, Y. Qiu, M. Gu, Z. Ge and J. He, *Energy Environ. Sci.*, 2020, **13**, 579–591.
39 P. Jood, M. Ohta, A. Yamamoto and M. G. Kanatzidis, *Joule*, 2018, **2**, 1339–1355.
40 P. Qiu, T. Mao, Z. Huang, X. Xia, J. Liao, M. T. Agne, M. Gu, Q. Zhang, D. Ren, S. Bai, X. Shi, G. J. Snyder and L. Chen, *Joule*, 2019, **3**, 1538–1548.
41 T. Xing, Q. Song, P. Qiu, Q. Zhang, M. Gu, X. Xia, J. Liao, X. Shi and L. Chen, *Energy Environ. Sci.*, 2021, **14**, 995–1003.
42 Y. Xing, R. Liu, J. Liao, C. Wang, Q. Zhang, Q. Song, X. Xia, T. Zhu, S. Bai and L. Chen, *Joule*, 2020, **4**, 2475–2483.
43 J. Yu, Y. Xing, C. Hu, Z. Huang, Q. Qiu, C. Wang, K. Xia, Z. Wang, S. Bai, X. Zhao, L. Chen and T. Zhu, *Adv. Energy Mater.*, 2020, **10**, 2000888.
44 E. Hatzikraniotis, K. T. Zorbas, I. Samaras, T. Kyratsi and K. M. Paraskevopoulos, *J. Electron. Mater.*, 2009, **39**, 2112–2116.
45 K. Imasato, M. Wood, S. Anand, J. J. Kuo and G. J. Snyder, *Adv. Energy Sustainability Res.*, 2022, DOI: **10.1002/aesr.202100208**.
46 C. Hu, K. Xia, C. Fu, X. Zhao and T. Zhu, *Energy Environ. Sci.*, 2022, **15**, 1406–1422.
47 J. J. Kuo, S. D. Kang, K. Imasato, H. Tamaki, S. Ohno, T. Kanno and G. J. Snyder, *Energy Environ. Sci.*, 2018, **11**, 429–434.
48 J. Mao, J. Shuai, S. Song, Y. Wu, R. Dally, J. Zhou, Z. Liu, J. Sun, Q. Zhang, C. dela Cruz, S. Wilson, Y. Pei, D. J. Singh, G. Chen, C.-W. Chu and Z. Ren, *Proc. Natl. Acad. Sci. U. S. A.*, 2017, **114**, 10548–10553.
49 R. He, D. Kraemer, J. Mao, L. Zeng, Q. Jie, Y. Lan, C. Li, J. Shuai, H. S. Kim, Y. Liu, D. Broido, C.-W. Chu, G. Chen and Z. Ren, *Proc. Natl. Acad. Sci. U. S. A.*, 2016, **113**, 13576–13581.
50 A. F. May, E. S. Toberer, A. Saramat and G. J. Snyder, *Phys. Rev. B: Condens. Matter Mater. Phys.*, 2009, **80**, 125205.
51 W.-S. Liu, Q. Zhang, Y. Lan, S. Chen, X. Yan, Q. Zhang, H. Wang, D. Wang, G. Chen and Z. Ren, *Adv. Energy Mater.*, 2011, **1**, 577–587.
52 M. Hong, K. Zheng, W. Lyv, M. Li, X. Qu, Q. Sun, S. Xu, J. Zou and Z.-G. Chen, *Energy Environ. Sci.*, 2020, **13**, 1856–1864.

